C. R. Mecanique 343 (2015) 533–544

Contents lists available at ScienceDirect

Comptes Rendus Mecanique

www.sciencedirect.com

Discrete simulation of fluid dynamics

Lattice Boltzmann formulation for flows with acoustic porous media

Chenghai Sun *, Franck Pérot, Raoyang Zhang, Phoi-Tack Lew, Adrien Mann, Vinit Gupta, David M. Freed, Ilya Staroselsky, Hudong Chen

Exa Corporation, 55 Network drive, Burlington, MA 01803, USA

ARTICLE INFO

Article history:
Received 3 March 2015
Accepted 17 July 2015
Available online 17 August 2015

Keywords:
Porous medium
Acoustics
Lattice Boltzmann

ABSTRACT

Porous materials are commonly used in various industrial systems such as ducts, HVAC, hoods, mufflers, in order to introduce acoustic absorption and to reduce the radiated acoustics levels. For problems involving flow-induced noise mechanisms and explicit interactions between turbulent source regions, numerical approaches remain a challenging task involving, on the one hand, the coupling between unsteady flow calculations and acoustics simulations and, on the other hand, the development of advanced and sensitive numerical schemes. In this paper, acoustic materials are explicitly modeled in lattice Boltzmann simulations using equivalent fluid regions having arbitrary porosity and resistivity. Numerical simulations are compared to analytical derivations as well as experiments and semi-empirical models to validate the approach.

1. Introduction

Porous media are widely used as sound-absorbing materials in various industries to reduce noise emission. For example, in modern turbofan engines, the inlet wall is treated with acoustic liners. Highway and railway noise barriers often use acoustic treatments for solving community noise issues. At a microscopic scale, propagation of sound in porous media is difficult to characterize because of the topological complexity of materials. At a macroscopic scale, some porous materials can be treated as regions of fluid that have modified properties relative to air [1], in the rigid or limp frame approximation. Sound propagation in such media is theoretically well characterized and can be expressed in the terms of two intrinsic frequency-dependent properties of the material: the characteristic impedance and the complex acoustic wavenumber. Various models for these properties based on experimental studies are presented in the literature. Under certain assumptions, a given sound propagation model in an absorbing material can be put in the form of locally-reacting, frequency-dependent, complex impedance at the interface between two different media. Such surface impedance models appear in most traditional numerical acoustics solvers such as Boundary Element Methods (BEM), Finite Elements Methods (FEM), and Statistical Energy Analysis (SEA) methods, and are relatively easy to implement as boundary conditions in the frequency domain.

For problems involving flow-induced noise, suitable CFD (Computational Fluid Dynamics) and/or CAA (Computational Aero-Acoustics) numerical methods are non-linear and often time-explicit. For a time-explicit solver, time-domain surface impedance boundary conditions could likewise allow the modeling of acoustic absorption due to porous materials [2]. Ozyoruk et al. [3] proposed a curve fitting of the experimental impedance data in the form of fractional polynomials in

* Corresponding author.
E-mail addresses: chenghai@exa.com (C. Sun), perot@exa.com (F. Pérot), raoyang@exa.com (R. Zhang), charlie@exa.com (P.-T. Lew), amann@exa.com (A. Mann), vinit@exa.com (V. Gupta), dmfreed@exa.com (D.M. Freed), ilya@exa.com (I. Staroselsky), hudong@exa.com (H. Chen).

http://dx.doi.org/10.1016/j.crme.2015.07.013
1631-0721/

the z-domain and derived an efficient implementation of the above impedance boundary condition in the time domain by using the z-transform. The simulations of the NASA Langley grazing flow tube case using this model [3–5] showed good agreement with experimental data. References [6,7] applied this scheme within a lattice Boltzmann method (LBM) flow solver and also showed similarly good correlations with the experiment. However, fitting the measurement data into this fractional polynomials might be challenging because causality, reality, and passivity listed by Rienstra [8] can not be always satisfied. Violation of these constrains could result in unphysical behavior or numerical instability.

Another possible approach is to model absorbing materials as equivalent fluid regions, such that sound waves travel through the materials. Analytical derivations show that the acoustic absorption is governed (or at least dominated) by the same physical mechanisms as the flow resistivity. As a consequence, the same equations used to achieve the correct flow resistivity for a particular porous material also achieve the correct acoustic impedance for that material. This approach was demonstrated valid for passive and homogeneous porous materials with high porosity near $\phi = 1.0$ [9].

In the present paper, in addition to the resistivity of porous materials, we account for the porosity as well in LBM, which greatly increases the applicability of the PM for solving acoustic and aero-acoustic problems.

The LBM has evolved over the last two decades as an alternative numerical method to traditional CFD [10–13]. The resulting compressible and unsteady solver is well suited for predicting a variety of complex flow physics [14,15] including aeroacoustics [16–20] and pure acoustics problems [21]. The present extension of porous media model with arbitrary porosity can be used to represent the flow resistivity of air filters, radiators, heat exchangers, evaporators, and other components that are encountered in simulating the flow through HVAC systems, vehicle engine compartments, and other applications.

In Section 2, numerical details related to LBM, and implementation of the porous media model is proposed. In Section 3, some background on acoustic propagation in porous media is described and analytical and semi-empirical models are given. In Section 4, two numerical setups are used to validate the predictions of the complex acoustic impedance and pressure losses of PM by comparison to analytical results. In the last section, some more realistic materials are investigated and further comparisons to experiments and semi-analytical models discussed.

2. LBM model for porous media

To model porous media we need to consider the PM resistance and the interface constraint.

The flow resistance σ of a porous medium is described by Darcy's law, which states that the pressure drop Δp is proportional to the flow velocity u and the thickness L of the PM, i.e.:

$$\Delta p = -\sigma u L \tag{1}$$

It can be generalized in 3-D in term of the resistance tensor $\boldsymbol{\sigma}$ of order 2 and velocity vector $\mathbf{u}$:

$$\nabla p = -\boldsymbol{\sigma} \cdot \mathbf{u} \tag{2}$$

In order to simulate the acoustic behavior in the PM, it is essential that the density and the velocity solved represent the real fluid density and velocity in the pores, excluding the solid portion of the porous media because the objective is to model the sound wave propagation in fluid. Meanwhile, the mass flux conservation should be satisfied at the fluid–PM interface. For non moving infinitely rigid solid micro-structure of PM it is expressed as:

$$(\rho u_n)_{\mathrm{f}} = \phi (\rho u_n)_{\mathrm{PM}} \tag{3}$$

with $u_n = \mathbf{u} \cdot \mathbf{n}$, $\mathbf{n}$ the interface normal vector, and ϕ the porosity. The indices f and PM represent fluid side and PM side, respectively.

Another aspect of interface is the interface resistance due to the presence of the solid structure. This interface resistance depends on the porosity, flow velocity and microscopic structure of the PM.

In the current study these PM related properties are incorporated in the 3-D 19-speed LBM (D3Q19) [11]:

$$f_i(\mathbf{x} + \mathbf{c}_i, t + \Delta t) = f_i(\mathbf{x}, t) - \frac{1}{\tau}\left(f_i(\mathbf{x}, t) - f_i^{\mathrm{eq}}(\mathbf{x}, t)\right) \tag{4}$$

with $f_i(\mathbf{x}, t)$ the particle density distribution function, τ is the single relaxation time, $\mathbf{c}_i$ the discrete particle velocity, and Δt the time step. The equilibrium distribution function $f_i^{\mathrm{eq}}(\mathbf{x}, t)$ has the following 3rd order form [22]:

$$f_i^{\mathrm{eq}}(\mathbf{x}, t) = \rho\, w_i \left[1 + \frac{\mathbf{c}_i \cdot \mathbf{u}}{T_0} + \frac{(\mathbf{c}_i \cdot \mathbf{u})^2}{2T_0^2} - \frac{\mathbf{u}^2}{2T_0} + \frac{(\mathbf{c}_i \cdot \mathbf{u})^3}{6T_0^3} - \frac{(\mathbf{c}_i \cdot \mathbf{u})\mathbf{u}^2}{2T_0^2}\right] \tag{5}$$

with $w_0 = 1/3$ for stop state, $w_i = 1/18$ for states in Cartesian directions and $w_i = 1/36$ for states in bi-diagonal directions. Here $T_0 = 1/3$ is the constant lattice temperature. The hydrodynamic quantities ρ and $\rho\,\mathbf{u}$ are the zero-th and first-order moments of the distribution functions, respectively:

$$\rho(\mathbf{x}, t) = \sum_i f_i(\mathbf{x}, t), \quad \rho(\mathbf{x}, t)\mathbf{u}(\mathbf{x}, t) = \sum_i \mathbf{c}_i f_i(\mathbf{x}, t) \tag{6}$$

In LBM, external forces can be included in the fluid dynamics by altering the local-instantaneous particle distributions during the collision step. This technique can be used for example to model buoyancy effects due to gravity, interacting force for multiphase flows [23], and reduction of speed of sound for high-Mach-number flows [24]. To achieve the porous media resistance defined by Darcy's law (Eq. (2)), an external force proportional to the local flow velocity is applied [25,26].

By the Chapman–Enskog expansion, the evolution of Eq. (4) matches the Navier–Stokes equations:

$$\frac{\partial \rho}{\partial t} + \nabla \cdot (\rho \mathbf{u}) = 0 \tag{7}$$

$$\frac{\partial \rho \mathbf{u}}{\partial t} + \nabla \cdot (\rho \mathbf{u}\mathbf{u}) = -\nabla p - \boldsymbol{\sigma} \cdot \mathbf{u} + \nabla \cdot \{\mu[\nabla \mathbf{u} + (\nabla \mathbf{u})^{\mathrm{T}}]\} \tag{8}$$

with viscosity, pressure and sound speed c_0 given by:

$$\mu = (\tau - 1/2)\rho, \quad p(\mathbf{x}, t) = c_0^2 \rho(\mathbf{x}, t), \quad c_0 = \frac{1}{\sqrt{3}} \frac{\Delta x}{\Delta t} \tag{9}$$

Δx is the unit lattice length.

In general, standard wall boundary conditions impose zero normal velocity for both no-slip and slip impermeable walls. Ref. [27] provides details of the generalized BCs for arbitrary geometry with extensive validations in [28,29]. For the fluid–PM interface, double-sided surfaces are employed like the sliding mesh algorithm [30]. The fluid can flow through the interface and a normal velocity satisfying Eq. (3) can be imposed at the interface. Following the algorithm [7], this is achieved by adding a corresponding mass flux on the interface [30].

For PM, since the velocity profiles inside pores can not be resolved, the viscous term of the Navier–Stokes equation can not be evaluated correctly using the resolved velocity gradients. In the present model, the viscous term is replaced by the Darcy's force $\boldsymbol{\sigma} \cdot \mathbf{u}$ to account for the viscous drag force or the friction caused by solid structures of the PM. Therefore the resistance effects due to complex solid structures inside the PM are modeled in terms of the Darcy's force and the viscous term (last term in Eq. (8)) is neglected. In the regular fluid region outside the PM the PM resistance disappears and the momentum equation (8) recovers the standard Navier–Stokes equation with viscous term. The system can describe both the regular fluids and PM.

3. Acoustic propagation in homogeneous porous media

Hersh and Walker [31] derived analytically the expression of the impedance introduced by the presence of similar porous media. Assuming non-viscous linear mechanisms and isothermal transformations, the 1-D mass and momentum equations in PM write:

$$\frac{\partial \rho'}{\partial t} = -\frac{\rho_0}{\phi} \frac{\partial u'}{\partial x} \tag{10}$$

$$\frac{\rho_0}{\phi} \frac{\partial u'}{\partial t} = -\frac{\partial p'}{\partial x} - \sigma \frac{u'}{\phi} \tag{11}$$

Assuming a simple harmonic solution, $\rho'(x,t) = \mathrm{e}^{\mathrm{i}\omega t}\rho'(x)$, $u'(x,t) = \mathrm{e}^{\mathrm{i}\omega t}u'(x)$, $p'(x,t) = \mathrm{e}^{\mathrm{i}\omega t}p'(x)$ and $p'(x) = Ae^{-(\alpha+i\beta)x}$, the $p'(x,t)$ and $u'(x,t)$ can be solved from Eqs. (10) and (11) and the equation of state. The material characteristic impedance Z is derived from the definition:

$$Z \equiv \frac{p'(x,t)}{u'(x,t)} = \frac{\rho_0 \omega \beta + \alpha \sigma}{\phi(\alpha^2 + \beta^2)} + \mathrm{i}\frac{\rho_0 \omega \alpha + \beta \sigma}{\phi(\alpha^2 + \beta^2)} \tag{12}$$

where α and β are functions of ω (as shown in Ref. [31]).

For the special case with $\phi = 1$ and $\sigma = 0$, Eqs (10) and (11) become the governing equations of sound propagation in air. Compared to the sound propagation in air, the velocity for PM is scaled up by $1/\phi$.

Considering the governing equations (7) and (8) resulting from the LBM model, since the density and the velocity solved represent the real fluid density and the velocity in the pores of the PM, the velocity is automatically scaled up. The linearization of these equations by assuming small perturbations $\rho = \rho_0 + \rho'$, $p = p_0 + p'$ and $u = u_0 + u'$ and neglecting the viscous term in the 1-D case recovers the Hersh–Walker's equations (10) and (11) with exactly the same PM resistance term. Hersh–Walker's model will be used as one of validations of our LBM PM model in next section.

4. Numerical results

Three validation studies are described in this section. First, a one-dimensional channel flow with a PM in the middle of the channel is used to validate the PM properties. Second, a digital normal impedance tube is used to verify that under pure acoustics (no-flow) conditions, the present implementation recovers the normal incidence impedance properties of the PM.

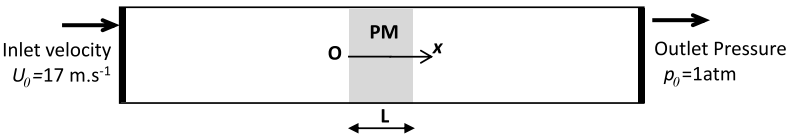

Fig. 1. Schematic representation of a 1-D channel setup.

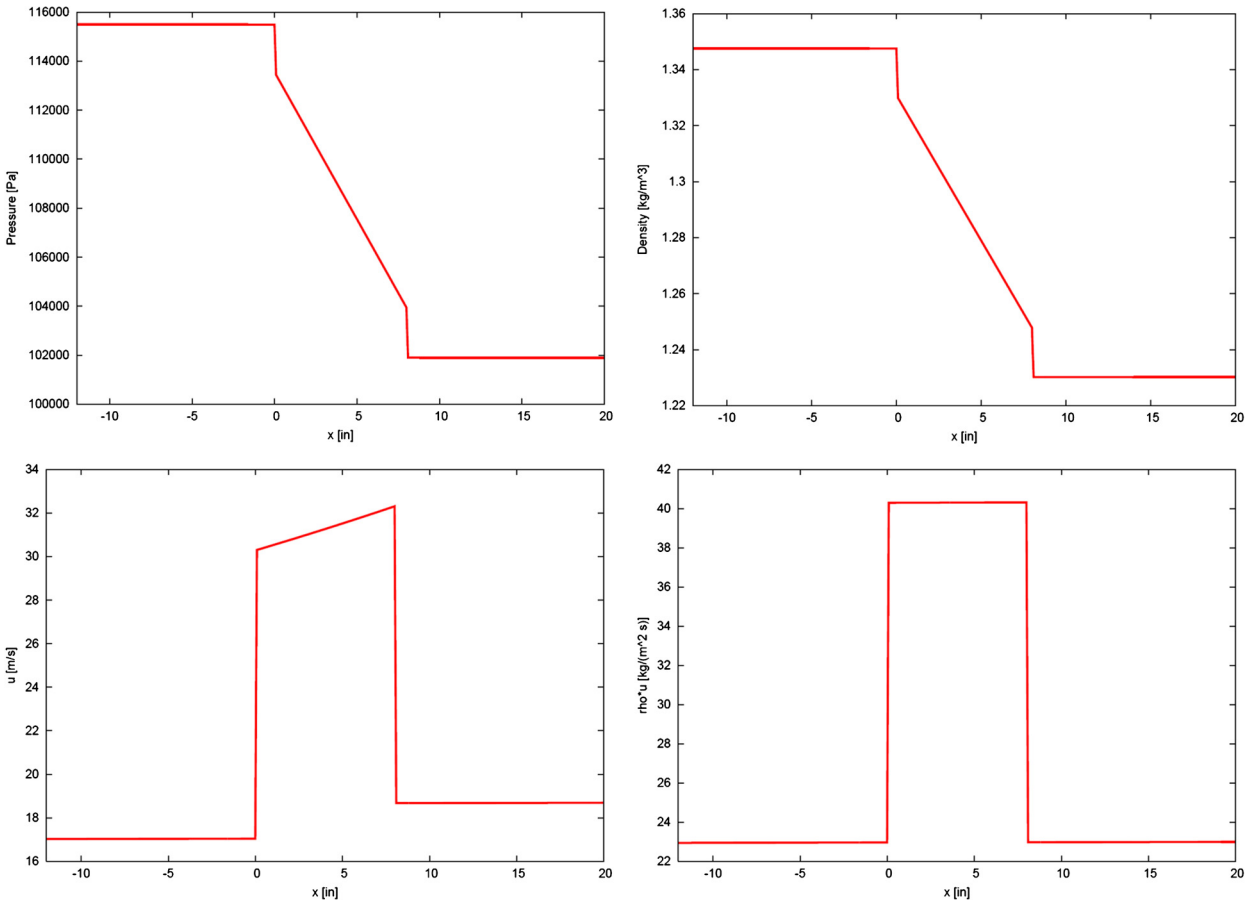

Fig. 2. (Color online.) Pressure, density, velocity, and ρu distribution along the channel.

The third study uses the NASA Langley grazing incidence impedance tube case [32], which includes a mean flow together with tangentially incident acoustics, and is a commonly used validation case in the open literature [3,6,7,4].

4.1. 1-D channel flow

The case setup is illustrated in Fig. 1. The channel width is $D = 2$ inches and 40 grid points are used across the channel. The NASA ceramic liner properties [32] are used to setup the PM properties. The liner is composed of micro circular channels with a ceramic filler arranged in honeycomb form. The micro channel diameter is $d_c = 0.64$ mm and the resulting liner porosity is $\phi = 0.57$. The resistivity is not provided in [32]. However, it can be calculated from the micro channel diameter, porosity and viscosity of air by [1]:

$$\sigma = \frac{32\,\mu}{d_c^2\,\phi} \tag{13}$$

which results in $\sigma = 2522\ \mathrm{kg\,m^{-3}\,s^{-1}}$ for air. At the inlet of the tube, a fixed velocity boundary condition at Mach number $M = 0.05$ is applied. At the outlet, the ambient pressure is imposed. The time step of simulation is $\Delta t = 2.112 \cdot 10^{-6}$ s. Fig. 2 shows the pressure, density, velocity and $\rho\,u$ distribution along the channel when the simulation reaches the steady state. The two pressure drops at the two PM interfaces are due to the interface pressure resistance. The resistivity inside PM should be equal to the pressure slope over inlet velocity according to Darcy's law. The measured resistivity from the

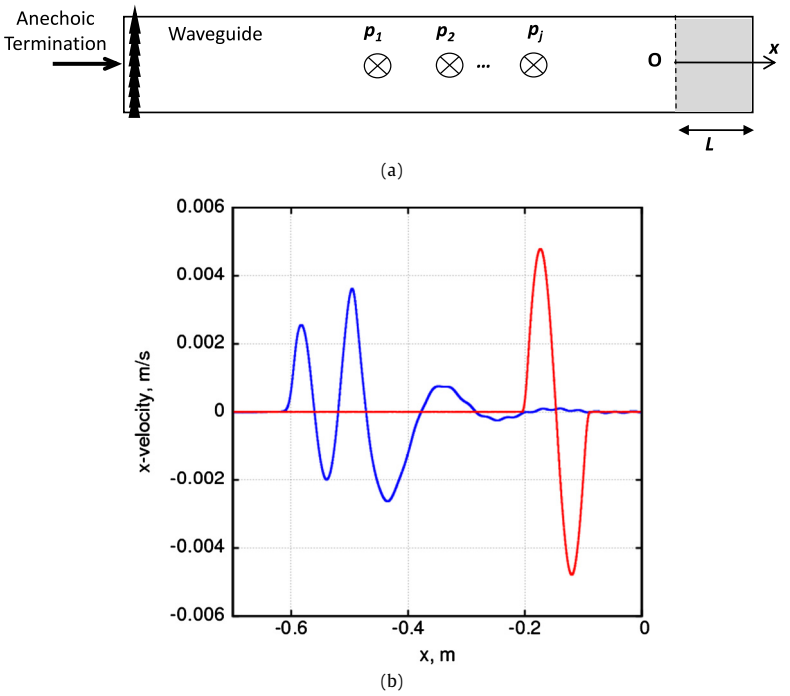

Fig. 3. (a): Schematic representation of the cylindrical Digital Normal Impedance Tube (DNIT). (b): Incident (red) and reflected (blue) velocity signals measured at $t = 2$ ms and $t = 3$ ms, respectively. (For interpretation of references to color in this figure caption, the reader is referred to the web version of this article.)

pressure slope is $\sigma = 2516\ \mathrm{kg\,m^{-3}\,s^{-1}}$, which is about 0.2% from the input resistivity value. While pressure and density degrease, velocity increases inside the PM, keeping ρu constant and therefore the flux constant. The validation of the achieved porosity is obtained by measuring the ratio of the momentum inside and outside the PM following Eq. (3). A value of $\phi = 0.57$ is obtained, which is in perfect agreement with Eq. (3).

4.2. Normal impedance tube

The complex impedance Z of a material can be experimentally measured in a Normal Impedance Tube (NIT) [33], and this setup is reproduced in the simulation. The geometry of the Digital Normal Impedance Tube (DNIT) proposed in this paper is composed of a 3-D cylindrical waveguide, in which the PM sample to be characterized is placed on the right end side, as represented in Fig. 3(a). The diameter of the waveguide is $D = 40$ mm and the walls are defined as frictionless. On the left end side of the waveguide, an anechoic termination is applied. The complex surface impedance and the absorption coefficient of the PM sample are calculated using a one-microphone method [34]. This method is based on the signal post-processing of pressure and velocity signals measured at different locations p_j inside the waveguide. The excitation consists in an incident single period sine signal in pressure and velocity propagating in the x-direction toward the PM sample. In the frequency domain, this excitation has a broadband content from a frequency $f = 10$ Hz to $f = 4000$ Hz corresponding to the frequency range over which the sample is characterized. In Fig. 3(b), the mechanisms occurring in the waveguide are schematized. At a time $t = 0$ s, the initial excitation propagates in $+x$-direction, as represented with the red signal in Fig. 3(b). When reaching the sample, this signal is reflected, transmitted and absorbed and after $t = 3$ ms, the resulting signal propagates in the $-x$-direction, as shown with the blue plot in Fig. 3(b). The anechoic termination implemented on the left side of the waveguide insures the full damping of the incoming signal in such a way no information travels back in the $+x$-direction.

From the incident and reflected pressure and velocity time histories recorded inside the DNIT, the normalized complex impedance $\hat{Z} = Z/Z_0$ with $Z_0 = \rho_0 c_0$ is derived as follows. At a given location p_j, the complex pressure $\bar{P^J}$ and velocity $\bar{V^J}$ are decomposed as follows:

$$\bar{P^J} = \bar{P_I^J} \exp(-\mathrm{i}kx_J) + \bar{P_R^J} \exp(\mathrm{i}kx_J) \tag{14}$$

$$\bar{V^J} = \frac{1}{\rho c}\left[\bar{P_I^J} \exp(-\mathrm{i}kx_J) + \bar{P_R^J} \exp(\mathrm{i}kx_J)\right] \tag{15}$$

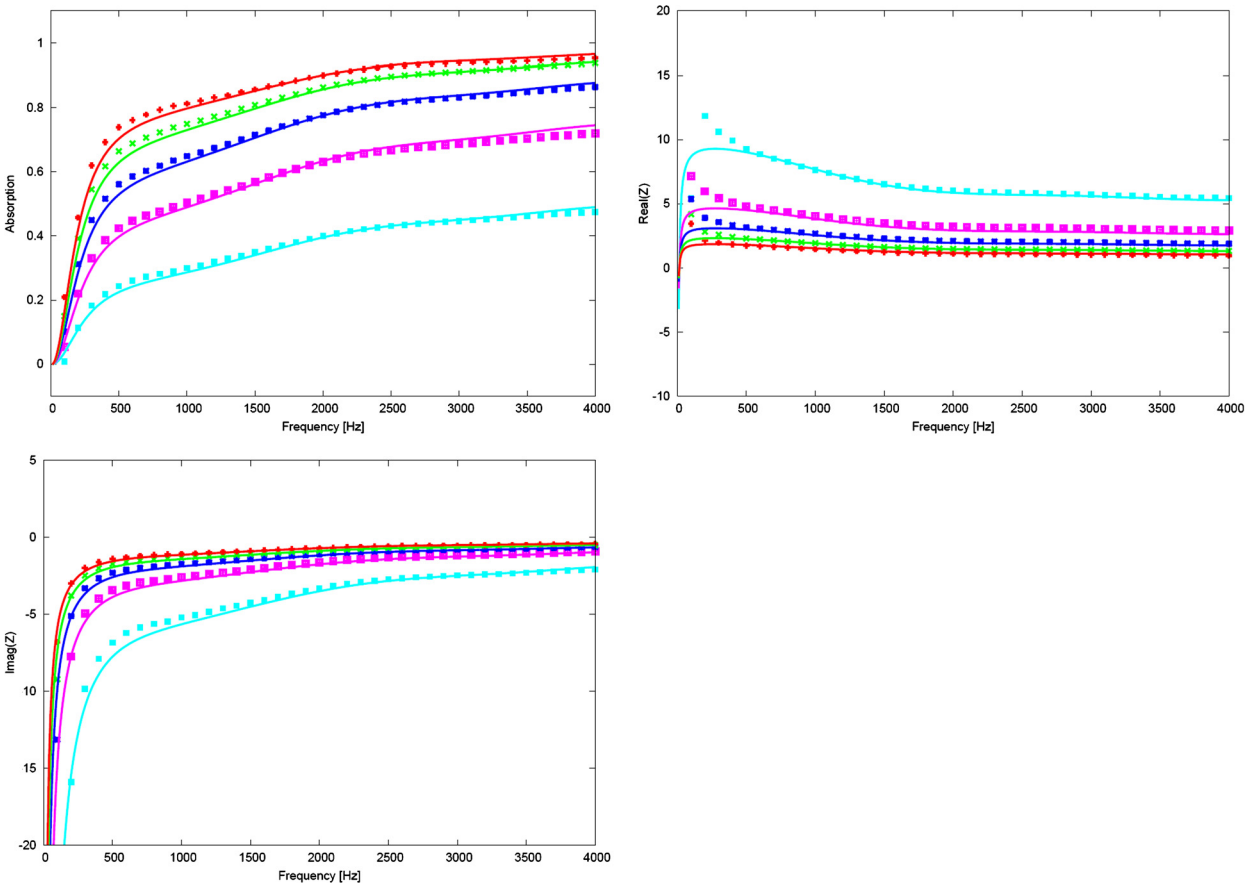

Fig. 4. Porosity dependence study. Absorption coefficient, real and Imaginary parts of the impedance as a function of the frequency. PM thickness is $L = 10$ cm and resistivity is $\sigma = 23{,}750\ \mathrm{kg\,m^{-3}\,s^{-1}}$. Lines: analytical solution. Symbols: LBM simulations. Cyan, pink, blue, green, and red correspond to $\phi = 0.2$, 0.4, 0.6, 0.8, and 1.0, respectively. (For interpretation of references to color in this figure caption, the reader is referred to the web version of this article.)

with k the spatial wavenumber, x_J the position of the probe relative in the waveguide, $\bar{P}_{\mathrm{I}}^{J}$ the incident complex pressure and $\bar{P}_{\mathrm{R}}^{J}$ the reflected complex pressure. The reflection coefficient is obtained by solving the system formed of Eqs. (14) and (15):

$$\bar{R}^{J} = \frac{\bar{P}_{\mathrm{R}}^{J}}{\bar{P}_{\mathrm{I}}^{J}} = \frac{\bar{P}^{J} - \rho c \bar{V}^{J}}{\bar{P}^{J} + \rho c \bar{V}^{J}} \exp(-2ikx_J) \tag{16}$$

The normalized impedance $\hat{Z}$ of the PM and the absorption coefficient α are given by the following expressions:

$$\hat{Z} = \frac{1 + \bar{R}^{J}}{1 - \bar{R}^{J}} \tag{17}$$

$$\alpha = 1 - \left|\bar{R}^{J}\right|^2 \tag{18}$$

The values of $\hat{Z}$ and α in the frequency domain are available at each location j. Since the results are observed to be independent with the location, the analysis performed at microphone $j = 7$ i.e. $x = -32.7$ mm are used in the rest of this study.

4.2.1. Normal impedance for felt

A porous medium of thickness $L = 10$ cm and resistivity $\sigma = 23{,}750\ \mathrm{kg\,m^{-3}\,s^{-1}}$ is used for validation. Several porosities, ranging from $\phi = 0.2$ to 1.0, are tested. The real part of the impedance should be positive, since the material is passive. Fig. 4 shows excellent agreement with the analytical solution based on the Hersh–Walker model [31] for all porosities, except the discrepancy of the real part at very low frequency, which can not be resolved due to the finite simulation time.

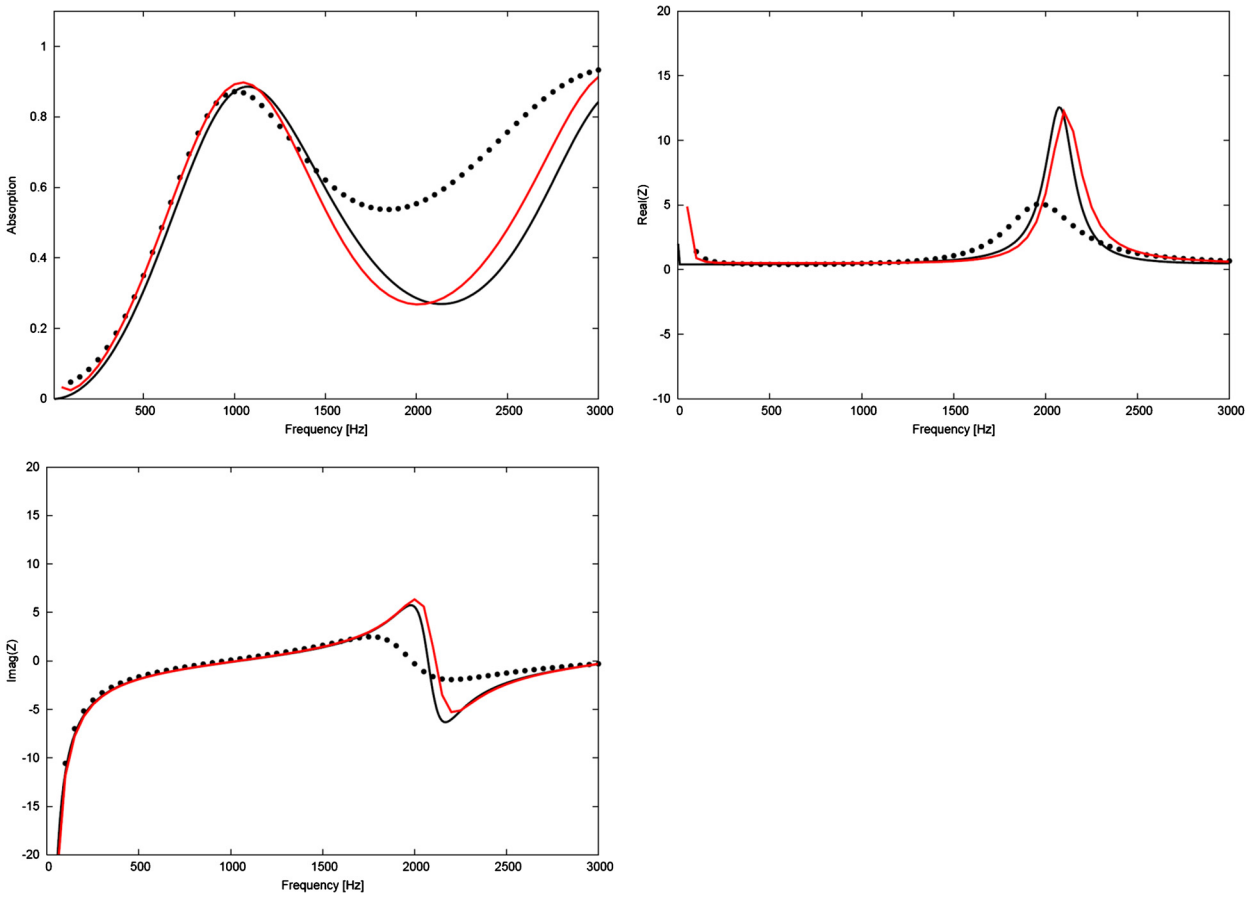

Fig. 5. Absorption coefficient, real and Imaginary parts of the impedance as a function of the frequency for NASA ceramic liner. PM thickness is $L = 8.25$ cm, porosity is $\phi = 0.57$, and resistivity is $\sigma = 2522\ \mathrm{kg\,m^{-3}\,s^{-1}}$. Black symbols: experimental data curve-fitted by [3]. Black lines: analytical solutions. Red lines: LBM simulations. (For interpretation of references to color in this figure caption, the reader is referred to the web version of this article.)

4.2.2. Normal impedance for NASA ceramic liner

Following the ceramic liner used in the experiment [32], the thickness of the PM imposed in the simulation is $L = 8.25$ cm. The same porosity $\phi = 0.57$ and resistivity $\sigma = 2522\ \mathrm{kg\,m^{-3}\,s^{-1}}$ are used as in Section 4.1. The results are compared to the data derived from the curve fitting of the measured complex surface impedance [3] and to the analytical solution based on the Hersh–Walker model.

As shown in Fig. 5, the result is again in good agreement with the analytical solution in the whole frequency range, which validates the numerical implementation of the model. Compared to experimental data, our simulation underestimated the absorption coefficient at a frequency around $f = 2000$ Hz, corresponding approximately to the resonance frequency for the given PM thickness. A possible reason might be that the current model misses the thermal effect and other porous media property effects, like the flexibility of the structure.

The overall satisfying comparison between experiments and predictions also highlight the correct modeling of absorption on the standing modes.

4.3. NASA Langley flow-impedance tube

The NASA Langley flow-impedance tube (also known as grazing flow tube) has been simulated following exactly the same setup as in experiments in [32]. The physical size of the tube is 33×2 inches. A ceramic liner of thickness $h = 8.25$ cm is embedded in the lower wall starting at 8.25 inches from the inlet and extending to 23.5 inches from the inlet (see Fig. 6). The porosity is $\phi = 0.57$. The resistivities in the x-direction $\sigma_x = \infty$ and in the y-direction $\sigma_y = 2522\ \mathrm{kg\,m^{-3}\,s^{-1}}$, which allows no flow in x-direction inside PM. Frictionless boundary conditions are imposed at the solid walls. A 661×41 2D grid is used, providing a number of points per wavelength NPPW $= 89$ at 3000 Hz. An acoustic plane wave is generated at the inlet:

$$p_{\mathrm{in}} = p_0 + \epsilon \sin(2\pi f t), \quad u_{\mathrm{in}} = u_0 + \frac{\epsilon}{\rho_0 c_0} \sin(2\pi f t), \quad v_{\mathrm{in}} = 0 \tag{19}$$

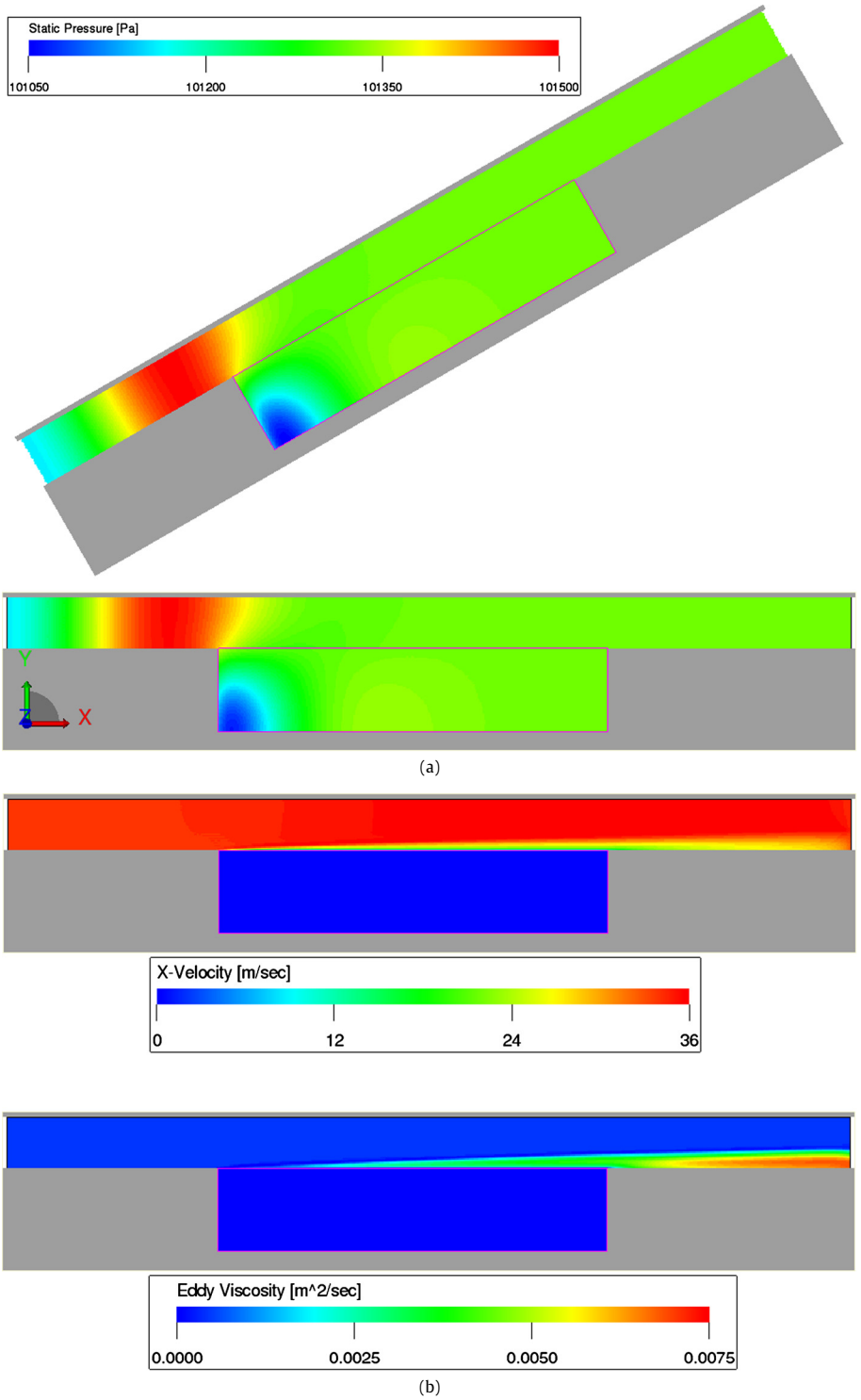

Fig. 6. (Color online.) (a): Instant snapshot of the static pressure field for ceramic liner grazing flow at $M = 0$. Comparison of lattice-aligned and 30-degree inclined channels. (b): Snapshots of x-velocity and eddy viscosity at $M = 0.1$.

with p_0 and ρ_0 the ambient pressure and density, ϵ and f the amplitude and frequency of the excitation, c_0 the speed of sound, and $u_0 = \mathrm{M}c_0$.

The sound pressure level (SPL) is calculated by:

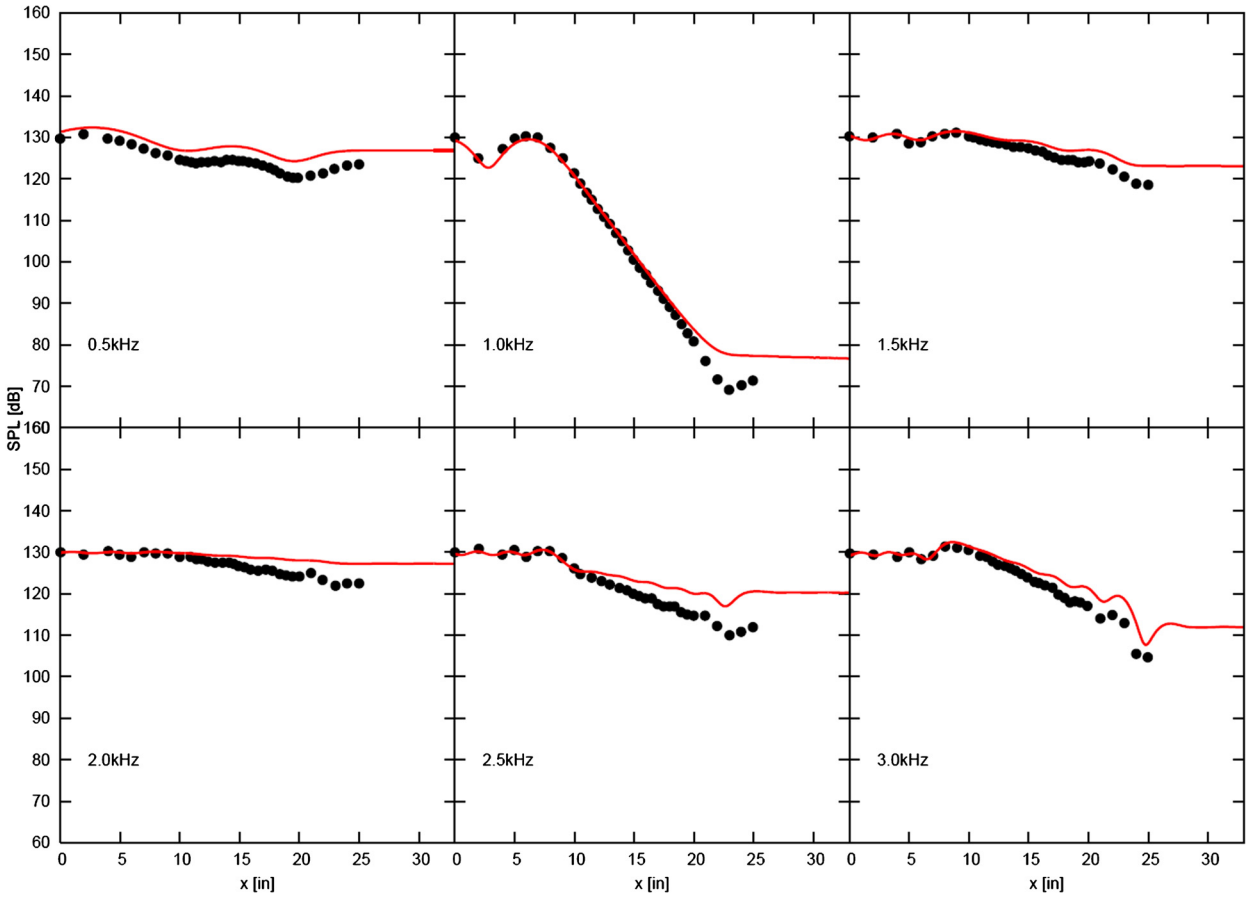

Fig. 7. (Color online.) Sound pressure level along the top wall for $M = 0., 0.1, 0.3$. Comparison of simulations (solid lines) with experimental data (symbols).

$$SPL = 20 \log\left(\frac{p_{\text{rms}}}{p_{\text{ref}}}\right), \quad p_{\text{rms}}^2 = \frac{1}{t_2 - t_1}\int_{t_1}^{t_2} (p - p_0)^2 \, \mathrm{d}t, \quad p_{\text{ref}} = 2 \cdot 10^{-5} \text{ Pa} \tag{20}$$

A sound level of SPL = 130 dB is set, for which $\epsilon = 89.44$ Pa. Two types of cases are tested: (1) lattice-aligned channel, (2) the channel inclined by 30 deg. For each type of case, the simulations are carried out at mean flow Mach numbers of $M = 0.0$, 0.1, and 0.3 and for frequencies ranging from $f = 0.5$ to 3.0 kHz with an increment of 0.5 kHz. SPL is measured along the upper wall at various locations and compared to experimental data [32].

Fig. 6 (a) shows instant snapshots of static pressure for the lattice-aligned and inclined channels at $M = 0$. Good agreement indicates the grid-orientation independence of the approach, which demonstrates the capability for simulations of complex geometries because the inclined channel walls and PM interface interact with volume elements of various sizes.

Fig. 6 (b) shows snapshots of x-velocity and eddy viscosity for the lattice-aligned channels at $M = 0.1$. Clearly, the boundary layer developed at the PM interface. This boundary layer is generated partially by the friction between the fluid from the fluid's side and the PM structure, and partially by the friction between the fluid from the fluid's side and that from the PM side, since the fluid inside the PM has zero x-velocity because of its infinite resistance in the x-direction.

Fig. 7 shows the comparison of the upper wall SPL results of lattice-aligned simulations with experimental data for $M = 0, 0.1$ and 0.3. At $M = 0.3$, the corresponding Reynolds number is $Re = 2 \cdot 10^5$. The symbols indicate the SPL measured on the upper wall. For the three configurations, the predicted results are in good agreement with the experimental data. The model implemented in LBM is thus shown to be able to capture the effect of the PM on absorption in the presence of a mean flow.

The case has 46,225 lattice nodes with approximately one half regular fluid nodes and one half PM nodes. The simulation time for a PM node is comparable to a regular fluid node (within 10% difference). The case consumes total 0.85 CPU hours on 4 Intel Xeon 3.07 GHz processors for 47,357 time steps, i.e. 0.016 s per time step.

To better resolve the development of the boundary layer and study the impact on acoustics, 89 points per wavelength are used and the results are presented here. We have also done the resolution study for $M = 0$ at 1 kHz. The acoustic results are almost unchanged between resolutions 44 and 89 points per wavelength, and they all agreed very well with those of

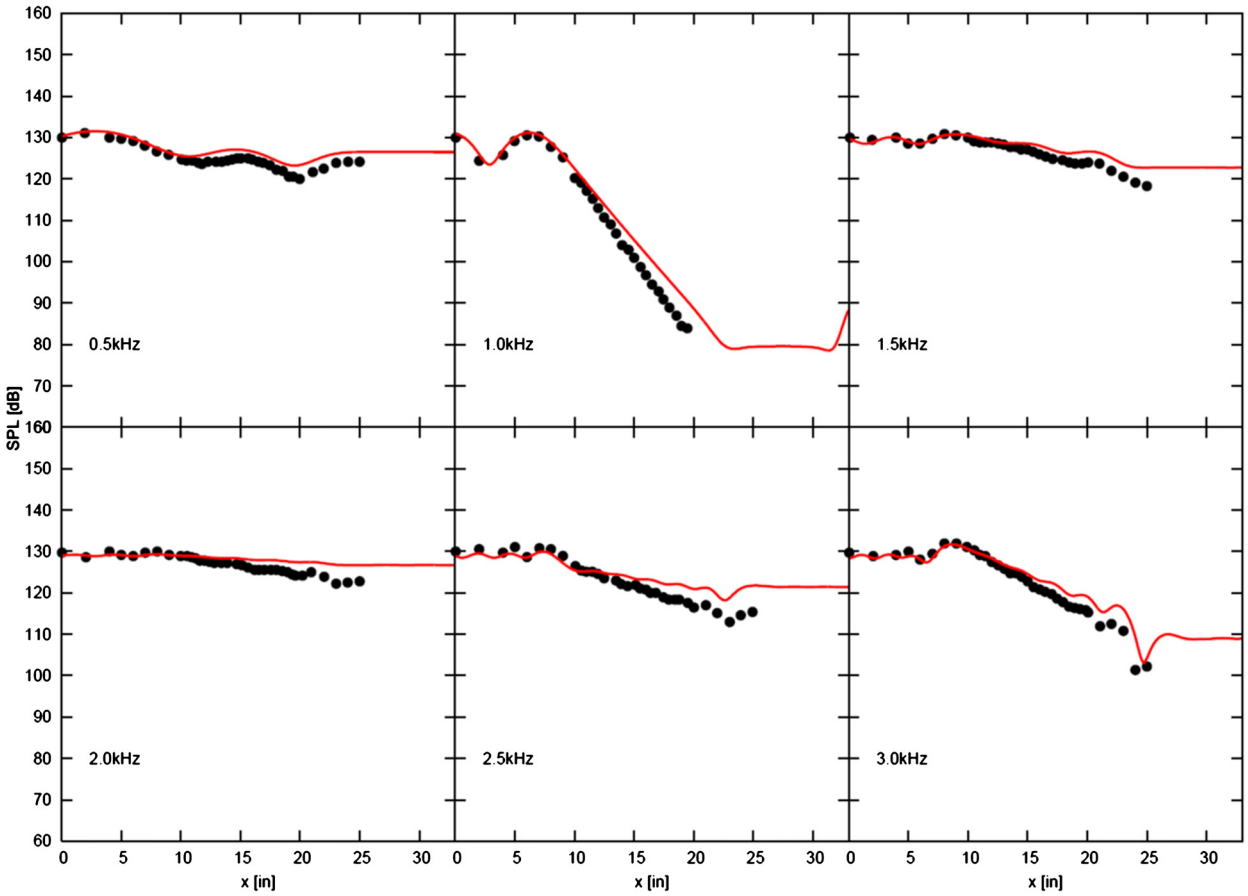

Fig. 7. (*continued*)

Ozyoruk's [3] and Delattre's [4] high-order schemes, using 25 to 30 points per wavelength. Our results of the resolution with 22 points per wavelength show only slight differences.

5. Discussion

The present LBM model for porous materials characterized by their resistivity and porosity introduces a PM resistance described by Darcy's law in the momentum equation, and precisely captures the porosity effect on the mass flux. As a consequence, the model takes both the hydrodynamics and acoustics behaviors of the PM into account simultaneously. In the pure fluid regions, the Darcy's force disappears and the standard Navier–Stokes equation applies. Therefore, the model can simulate not only hydrodynamic problems but also acoustics in any combination of pure fluid, PM and walls encountered in real industrial applications. Our model simply solves a system defined by the equations (7)–(9) with a constraint (Eq. (3)) without using any other models. Neither surface impedance model nor frequency-dependent input parameters are used in our model. The acoustic properties are calculated from the simulated pressure distribution directly after the simulations.

The capability for solving for a complex main flow and acoustic damping in the presence of PM at the same time opens possibility for many practically important applications where the noise is induced by vortices that are in turn generated by shear layers. Examples include flow induced noise controls such as jet noise from an aircraft engine, car sunroof buffeting, fan noises, etc.

The channel flow test case demonstrates the correct hydrodynamic behavior of the PM. The normal impedance tube cases showed very satisfying agreement with the analytical solution of sound wave propagation in a PM. The present model is much more powerful than the analytical model in the sense that it is applicable to any complex 3-D PM and wall geometries, and is not limited to small perturbations and to normal incidence waves.

The NASA grazing flow test case showed good agreement with the experimental data, and is at least as accurate as surface-based impedance boundary condition approaches [3,4,6,7]. The commonly used impedance boundary conditions is formulated as a relation between pressure and velocity in the frequency space that is prescribed at the PM interface. When using this method to account for the PM effect, the thickness of PM is completely ignored [3,4,6,7]. It is well known that transferring this impedance boundary condition from the frequency to the time domain has to satisfy a number of

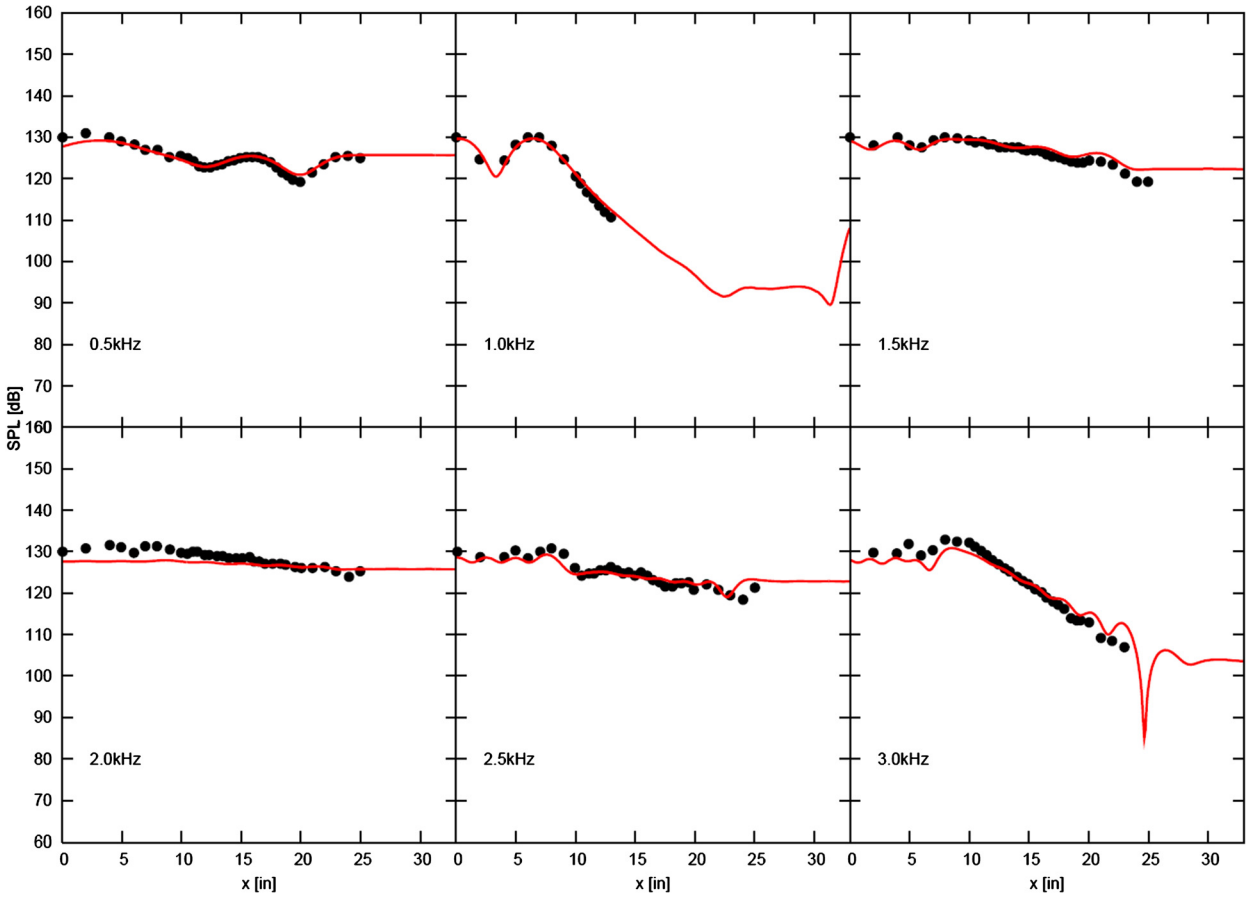

Fig. 7. (*continued*)

constrains [8]. These conditions are difficult to satisfy in a general case, their violation immediately causes instability of the method due to ill-posedness in the time domain. In contrast, our model naturally avoids the stability problem by directly solving in the time domain the PM equations that naturally damp acoustic waves.

Both the normal impedance tube and the grazing flow with ceramic liner showed how little information is required to get correct absorption behaviors of the porous material. The ceramic liner setup used only the geometric information of the porous material: porosity and diameter of the porous micro channels, from which the PM resistivity was calculated, together with the thickness of the PM layer. In a general setup, porosity, resistivity and PM geometry are needed. In some application cases, these information may not be available, and instead, the absorption coefficient is a priori characterized. A regression method as described in [9] can provide an equivalent modeling of the system and lead to broad range of applications.

References

[1] J.-F. Allard, N. Atalla, Propagation of Sound in Porous Media, second edition, Wiley, 2009.
[2] C.K.W. Tam, L. Auriault, Time-domain impedance conditions for computational aeroacoustics, AIAA J. 34 (1996) 917.
[3] Y. Ozyoruk, L. Long, M. Jones, Time-domain numerical simulation of a flow-impedance tube, J. Comput. Phys. 146 (1998) 29–57.
[4] G. Delattre, E. Manoha, S. Redonnet, P. Sagaut, Time-domain simulation of sound absorption on curved wall, in: 13th AIAA/CEAS Aeroacoustics Conference, Rome, Italy, 2007, AIAA-2007-3493.
[5] X.Y. Li, X.D. Li, Construction and validation of a broadband time domain impedance boundary condition, in: 17th AIAA/CEAS Aeroacoustics Conference, Portland, Oregon, 2011, AIAA-2011-2870.
[6] A. Toutant, P. Sagaut, Lattice Bolzmann simulatons of impedance tube flow, Comput. Fluids 38 (2009) 458–465.
[7] C. Sun, F. Pérot, R. Zhang, D.M. Freed, H. Chen, Impedance boundary condition for lattice Boltzmann model, Commun. Comput. Phys. 13 (2013) 757–768.
[8] S.W. Rienstra, 1-D reflection at an impedance wall, J. Sound Vib. 125 (1988) 43–51.
[9] F. Pérot, D.M. Freed, A. Mann, Acoustic absorption of porous materials using LBM, in: 19th AIAA/CEAS Aeroacoustics Conference, Berlin, May 2013, AIAA-2013-2070.
[10] H. Chen, S. Chen, W. Matthaeus, Recovery of the Navier–Stokes equation using a lattice-gas Boltzmann method, Phys. Rev. A 45 (1992) 5339–5342.
[11] Y.H. Qian, D. d'Humières, P. Lallemand, Lattice BGK models for Navier–Stokes equation, Europhys. Lett. 17 (1992) 479–484.
[12] R. Benzi, S. Succi, M. Vergassola, Lattice Boltzmann equation: theory and applications, Phys. Rep. 222 (1992) 145–197.
[13] S. Chen, G.D. Doolen, Lattice Boltzmann method for fluid flows, Annu. Rev. Fluid Mech. 30 (1998) 329–364.
[14] H. Chen, S. Kandasamy, S. Orszag, R. Shock, S. Succi, V. Yakhot, Extended Boltzmann kinetic equation for turbulent flows, Science 301 (2003) 633–636.

[15] H. Chen, S. Orszag, I. Staroselsky, S. Succi, Expanded analogy between Boltzmann kinetic theory of fluid and turbulence, J. Fluid Mech. 519 (2004) 307–314.
[16] B. Crouse, G. Balasubramanian, G. Senthooran, D.M. Freed, K.D. Ih, S.R. Shin, Investigation of gap deflector efficiency for reduction of sunroof buffeting, in: SAE Conference 2009-01-2233, 2009.
[17] F. Pérot, M. Meskine, S. Vergne, Investigation of the statistical properties of pressure loadings on real automotive side glasses, in: 13th AIAA/CEAS Aeroacoustics Conference, Miami, Florida, 2009, AIAA-2009-3402.
[18] S. Senthooran, B. Crouse, G. Balasubramanian, D. Freed, S.R. Shin, K.D. Ih, Effect of surface mounted microphones on automobile side glass pressure fluctuations, in: Proc. 7th MIRA Intl. Vehicle Aerodynamics Conf., Richoh Arena, UK, Oct. 22, 2008.
[19] J.L. Adam, D. Ricot, F. Dubief, C. Guy, Aeroacoustic simulation of automotive ventilation outlets, in: Proc. Acoustics 08 Conference, Paris, June 29, 2008.
[20] F. Pérot, M.S. Kim, D.M. Freed, L. Dongkon, K.D. Ih, M.H. Lee, Direct aeroacoustics prediction of ducts and vents noise, in: 14th AIAA/CEAS Aeroacoustics Conference, Stockhlom, 2010, AIAA paper 2010-3724.
[21] A. Laffite, F. Pérot, Investigation of the noise generated by cylinder flows using a direct lattice-Boltzmann approach, in: 13th AIAA/CEAS Aeroacoustics Conference, Miami, Florida, 2009, AIAA 2009-3268.
[22] H. Chen, X. Shan, Fundamental conditions for N-th-order accurate lattice Boltzmann models, Physica D 237 (2008) 2003–2008.
[23] X. Shan, H. Chen, Simulation of non-ideal gases and liquid–gas phase transitions by lattice Boltzmann equation, Phys. Rev. E 49 (1994) 2941–2948.
[24] X. Nie, X. Shan, H. Chen, Lattice-Boltzmann finite-difference hybrid simulation of transonic flow, in: 47th AIAA Aerospace Science Meeting Including The Horizons Forum and Aerospace Exposition, Orlando, FL, USA, 2009, AIAA 2009-139.
[25] D.M. Freed, Lattice-Bolzmann method for macroscopic porous media modeling, Int. J. Mod. Phys. 9 (1998) 1491–1505.
[26] J. Bear, Dynamics of Fluids in Porous Media, Dover, New York, 1988.
[27] H. Chen, C. Teixeira, K. Molving, Realization of fluid boundary conditions via discrete Boltzmann dynamics, Int. J. Mod. Phys. C 9 (1998) 1281–1292.
[28] Y. Li, R. Shock, R. Zhang, H. Chen, Numerical study of flow past an impulsively started cylinder by the lattice-Boltzmann method, J. Fluid Mech. 519 (2004) 273–300.
[29] R. Kotapati, R. Shock, H. Chen, Lattice-Boltzmann simulations of flow over backward-facing inclined steps, Int. J. Mod. Phys. C 25 (2014) 1340021.
[30] R. Zhang, C. Sun, Y. Li, R. Satti, R. Shock, J. Hoch, H. Chen, Lattice Boltzmann approach for local reference frames, Commun. Comput. Phys. 9 (2011) 1193–1205.
[31] A.S. Hersh, B. Walker, Acoustical behavior of homogeneous bulk materials, in: 6th AIAA Aeroacoustics Conference, 1980, AIAA-80-0986.
[32] T.L. Parrott, W.R. Watson, M.G. Jones, Experimental validation of a two-dimensional shear-flow model for determining acoustic impedance, NASA Technical Paper 2679, 1987, pp. 1–46.
[33] M.J. Jones, P.E. Stiede, Comparison of methods for determining specific acoustic impedance, J. Acoust. Soc. Amer. 101 (1997) 2694.
[34] K. Habibi, L. Mongeau, Numerical simulation of sound absorption by turbulent jet flows using the lattice-Boltzmann method, Internoise 2012, paper No. 422, New York, 2012.